

Preconditioned lattice Boltzmann method for steady flows: A noncascaded central-moments-based approach

Alessandro De Rosi^{*}*Department of Biomedical Engineering Technion-Israel Institute of Technology, 32000 Haifa, Israel*

(Received 3 June 2017; revised manuscript received 31 August 2017; published 18 December 2017)

We present a concise yet effective central-moments-based lattice Boltzmann method with an accelerated convergence to the steady state through preconditioning. It is demonstrated that the proposed scheme reduces to a slight modification of the unaccelerated one, as the preconditioning affects only the equilibrium state. Different from previous efforts carried out within the lattice Boltzmann community, the present scheme is built on an original model. In fact, the corresponding collision operator loses the pyramidal orchestrated nature that is typical of the cascaded scheme, hence we coin the name “noncascaded.” Our model is very general, characterized by highly intelligible formulations, simple to implement, and it can be derived for any lattice velocity space.

DOI: [10.1103/PhysRevE.96.063308](https://doi.org/10.1103/PhysRevE.96.063308)

I. INTRODUCTION

Originated from the lattice gas automata, the lattice Boltzmann method (LBM) is nowadays a consolidated approach to simulate viscous flows [1–3]. Instead of solving the macroscopic-based Navier-Stokes equations, the problem reduces to predict the mesoscopic motion of distributions (or populations) of fictitious particles, namely f_i , colliding and streaming along the link of a fixed Cartesian lattice. The governing lattice Boltzmann equation (LBE) is explicit in time and it recovers the solution of the Navier-Stokes equations for incompressible flow with second-order of accuracy [4]. In the classical formulation, the collision process leads populations to relax to an equilibrium state with a common unique rate and it is known as the Bhatnagar-Gross-Krook (BGK) approximation [5]. Among the most attractive features, the algorithmic simplicity of the BGK LBM has promoted its phenomenal success.

The LBM is an intrinsically time-dependent scheme. As a consequence, it has been widely adopted to simulate unsteady phenomena, e.g., suspensions flows, turbulence, and fluid-structure interaction [6–11]. Unfortunately, it requires a very large number of time steps to obtain steady-state predictions [12] as it needs to pass through a transient phase. This drive-through-transient penalty can dramatically impact on the computational cost. Moreover, aiming at recovering the solution of the incompressible Navier-Stokes equations, one is tempted to carry out simulations at a Mach number (Ma) as small as possible. In fact, the LBE introduces a compressibility error that is proportional to Ma^2 [13]. However, at low Ma , a very large disparity arises between the speed of sound and the fluid convection, thus further delaying the reach of the steady state. A possible solution to this issue can be found in time-independent LB schemes [14–16]. Moreover, the possibility to use larger time steps has been discussed in [17–21] by means of an implicit LBE. However, the price to pay is the loss of the natural simplicity of the BGK scheme.

From a more formal viewpoint, one should consider that the LBE is hyperbolic with an explicit time marching scheme. Vanishing Mach scenarios correspond to high values of the

condition number, i.e., the ratio of the maximum to minimum eigenvalues of the hyperbolic system, that scales as $\sim Ma^{-1}$. The application of a preconditioner in fluid dynamics has proved to reduce the condition number, as it is able to damp the difference in the propagation speed of two quantities [22]. Pointing out this effect, Guo *et al.* [23] suggested to relax populations to an equilibrium state modified by a factor γ , with $0 < \gamma \leq 1$. This seminal contribution demonstrated that it is possible to drastically accelerate the convergence to steady state, while keeping all the attractive characteristics typical of the BGK LBM. Later, Premnath *et al.* [24] extended this approach to multiple-relaxation time (MRT) in the presence of forcing terms. Another MRT effort has been carried out by Izquierdo and Fuego [25], who also have proposed optimal values of the preconditioning factor [26]. Interestingly, Izquierdo and Fuego [26] indicated that a preconditioning technique should possess some highly desirable properties, such as an ideal acceleration ratio, a general formulation, and a simple implementable procedure. Moreover, it should preserve the collide-and-stream process for a given LB model. The aim of the present paper is to propose an approach exhibiting all these compelling features.

Here, we derive a LB scheme with preconditioning in the framework of a collision operator written in terms of central moments (CMs). In 2006, Geier *et al.* [27] introduced the so-called “cascaded” collision operator. This name comes from the particular hierarchical structure of the kernel, where the postcollision state of a certain moment at a given order depends on lower order ones, and not vice versa. Building on this concept, many works demonstrated that the cascaded operator can impressively enhance the stability of the LBM [27–35]. Within this approach, a very recent and notable contribution has been proposed by Hajabdollahi and Premnath [36] to improve the low-Mach steady-state convergence of the LBM. With respect to this valuable effort, we adopt a recently introduced nonorthogonal CM-based model that loses the pyramidal topological pattern of the collision process [37–40]. Therefore, it can be interpreted as a “noncascaded” CM-based approach. Furthermore, our model entails an intelligible analytical formulation that can be easily extended to any lattice velocity space, as demonstrated. Moreover, the practical implementation does not represent a hard task. In addition, we demonstrate that preconditioned raw-moments-based kernels can be derived as a particular case of our algorithm. Numerical

^{*}derosis.alessandro@icloud.com

tests highlight the very good numerical properties in terms of accuracy and convergence of our approach, with the preconditioning factor being able to remarkably accelerate the convergence to the steady state.

The rest of the paper is organized as follows. In Sec. II, preconditioned approaches are discussed with particular emphasis on the proposed noncascaded model. Then, results from numerical tests are shown in Sec. III. Finally, some conclusions are drawn in Sec. IV.

II. PRECONDITIONED CMS-BASED LBM

In this section, first the BGK model by Guo *et al.* [23] is recalled. Then, our proposed scheme is presented.

A. BGK formulation by Guo *et al.*

Let us focus on a two-dimensional context, where the D2Q9 LB model is adopted to predict the evolution of the populations $|f_i\rangle = [f_0, f_1, f_2, f_3, f_4, f_5, f_6, f_7, f_8]^\top$. Here and henceforth, let us use the symbols $|\bullet\rangle$ and \top to denote a column vector and the transpose operator, respectively. Moreover, the superscripts *eq* and \star indicate equilibrium and postcollision quantities, respectively. In addition, the index i varies as $i \in [0 : l]$, with $l = 8$ in this case. Lattice directions, $\mathbf{c}_i = [c_{xi}, c_{yi}]$, are defined as

$$\begin{aligned} |c_{xi}\rangle &= [0, 1, 0, -1, 0, 1, -1, -1, 1]^\top, \\ |c_{yi}\rangle &= [0, 0, 1, 0, -1, 1, 1, -1, -1]^\top. \end{aligned} \quad (1)$$

Let us denote the Eulerian basis as $\mathbf{x} = [x, y]$, the time as t , and the time step as Δt . The BGK LBE reads as follows:

$$f_i(\mathbf{x} + \Delta t \mathbf{c}_i, t + \Delta t) = f_i(\mathbf{x}, t) + \omega [f_i^{eq}(\mathbf{x}, t) - f_i(\mathbf{x}, t)], \quad (2)$$

that as usual is divided into two parts, namely *collision*,

$$f_i^\star(\mathbf{x}, t) = f_i(\mathbf{x}, t) + \omega [f_i^{eq}(\mathbf{x}, t) - f_i(\mathbf{x}, t)], \quad (3)$$

and *streaming*,

$$f_i(\mathbf{x} + \Delta t \mathbf{c}_i, t + \Delta t) = f_i^\star(\mathbf{x}, t), \quad (4)$$

where ω is the relaxation frequency. To lighten the notation, the dependence on space and time is implicitly assumed in the rest of this section. The equilibrium state is defined as

$$f_i^{eq} = w_i \rho \left[1 + \frac{\mathbf{c}_i \cdot \mathbf{u}}{c_s^2} + \frac{(\mathbf{c}_i \cdot \mathbf{u})^2}{2\gamma c_s^4} - \frac{\mathbf{u} \cdot \mathbf{u}}{2\gamma c_s^2} \right], \quad (5)$$

where $c_s = 1/\sqrt{3}$ is the lattice speed of sound, $\mathbf{u} = [u_x, u_y]$ is the velocity vector, and the weighting factors are $w_0 = 4/9$, $w_{1\dots 4} = 1/9$ and $w_{5\dots 8} = 1/36$ [13]. As usual, macroscopic variables are available locally as the zeroth and first order moments of the particle distribution functions, i.e.,

$$\rho = \sum_i f_i, \quad \rho \mathbf{u} = \sum_i f_i \mathbf{c}_i, \quad (6)$$

respectively.

By performing the Chapman-Enskog expansion, Guo *et al.* [23] demonstrated that Eq. (2) recovers the preconditioned

Navier-Stokes equations, i.e.,

$$\begin{aligned} \frac{\partial \rho}{\partial t} + \nabla \cdot (\rho \mathbf{u}) &= 0, \\ \frac{\partial (\rho \mathbf{u})}{\partial t} + \frac{1}{\gamma} \nabla \cdot (\rho \mathbf{u} \mathbf{u}) &= -\frac{1}{\gamma} \nabla p^\dagger + \frac{1}{\gamma} \nabla \cdot (\rho \nu \mathbf{S}), \end{aligned} \quad (7)$$

where $p^\dagger = \gamma c_s^2 \rho$ is the pressure and $\mathbf{S} = \nabla \mathbf{u} + (\nabla \mathbf{u})^\top$.

In order to elucidate the role of the preconditioning factor γ , Eqs. (7) can be rewritten as

$$\frac{\partial \mathbf{Q}}{\partial t} + \mathbf{P} \mathbf{A} \frac{\partial \mathbf{Q}}{\partial x} + \mathbf{P} \mathbf{B} \frac{\partial \mathbf{Q}}{\partial y} = \mathbf{P} \mathbf{R}, \quad (8)$$

with \mathbf{R} is a term related to the viscosity, $\mathbf{P} = \text{diag}(1, \gamma^{-1}, \gamma^{-1})$ is a preconditioning matrix, $\mathbf{A} = \partial \mathbf{E} / \partial \mathbf{Q}$, and $\mathbf{B} = \partial \mathbf{F} / \partial \mathbf{Q}$. The remaining quantities are defined as $\mathbf{Q} = [\rho, \rho u_x, \rho u_y]$, $\mathbf{E} = [\rho u_x, \rho(u_x^2 + c_s^2), \rho u_x u_y]^\top$, and $\mathbf{F} = [\rho u_y, \rho u_x u_y, \rho(u_y^2 + c_s^2)]^\top$. The stiffness of the problem can be estimated by computing the eigenvalues λ of the preconditioning matrix $\mathbf{P} \mathbf{A}$, i.e.,

$$\lambda(\mathbf{P} \mathbf{A}) = \frac{1}{\gamma} [u_x, u_x - c_s^\dagger, u_x + c_s^\dagger], \quad (9)$$

with $c_s^\dagger = u_x \sqrt{1 - \gamma + (\gamma c_s / u_x)^2}$. It can be immediately noted that $\gamma = 1$ leads to $c_s^\dagger \equiv c_s$, thus implying a very large condition number for small values of Ma. Conversely, one can achieve that $c_s^\dagger \rightarrow u_x$ if $\gamma \rightarrow 0$. In other words, it is possible to reduce the disparity between the fluid propagation and the speed of the acoustic waves by properly tuning the parameter γ . By adopting this method, a numerical simulation is characterized by two Mach numbers: a real one, $\text{Ma} = u/c_s$, and an effective one, $\text{Ma}^\dagger = u/c_s^\dagger$, where u is a certain characteristic velocity. Notice that the two dimensionless quantities are related as $\text{Ma}^\dagger = \sqrt{\gamma} \text{Ma}$.

Preconditioning for steady-state solutions. By collecting the parameter γ , the preconditioned Navier-Stokes equations can be equivalently rewritten as

$$\begin{aligned} \frac{\partial \rho}{\partial t} + \nabla \cdot (\rho \mathbf{u}) &= 0, \\ \gamma \frac{\partial (\rho \mathbf{u})}{\partial t} + \nabla \cdot (\rho \mathbf{u} \mathbf{u}) &= -\nabla p^\dagger + \nabla \cdot (\rho \nu \mathbf{S}), \end{aligned} \quad (10)$$

where the existence of a preconditioned time derivative stems out. In its discrete form and given the fact that usually $\gamma \ll 1$, the preconditioned time step may be some order of magnitude higher than the unpreconditioned one. Consistently, it may play a detrimental effect on the temporal accuracy of the explicit time marching scheme, because the CFL condition may be violated. Conversely, the incidence of the parameter γ annihilates at the steady state, where the time derivative vanishes (i.e., $\frac{\partial \mathbf{u}}{\partial t} \equiv 0$) and the method recovers correctly the steady-state Navier-Stokes equations. Therefore, the preconditioned LB methods presented in [23,36] focus on stationary solutions, as well as the algorithm proposed in the following.

B. Present two-dimensional model

In order to derive a CMS-based formulation, let us shift the lattice directions by the local fluid velocity [27]:

$$|\bar{c}_{xi}\rangle = |c_{xi} - u_x\rangle, \quad |\bar{c}_{yi}\rangle = |c_{yi} - u_y\rangle. \quad (11)$$

Let us adopt the following basis:

$$\tilde{T} = [\tilde{T}_0, \dots, \tilde{T}_i, \dots, \tilde{T}_8], \quad (12)$$

with

$$\begin{aligned} |\tilde{T}_1\rangle &= |\bar{c}_{ix}\rangle, & |\tilde{T}_2\rangle &= |\bar{c}_{iy}\rangle, \\ |\tilde{T}_3\rangle &= |\bar{c}_{ix}^2 + \bar{c}_{iy}^2\rangle, & |\tilde{T}_4\rangle &= |\bar{c}_{ix}^2 - \bar{c}_{iy}^2\rangle, \\ |\tilde{T}_5\rangle &= |\bar{c}_{ix}\bar{c}_{iy}\rangle, & |\tilde{T}_6\rangle &= |\bar{c}_{ix}^2\bar{c}_{iy}\rangle, \\ |\tilde{T}_7\rangle &= |\bar{c}_{ix}\bar{c}_{iy}^2\rangle, & |\tilde{T}_8\rangle &= |\bar{c}_{ix}^2\bar{c}_{iy}^2\rangle. \end{aligned} \quad (13)$$

The column vector $|\tilde{T}_0\rangle$ possesses nine unitary components. Notice that the matrix \tilde{T} allows us to perform the transformation from populations to moments. Then, a suitable set of central moments is represented by

$$|k_i\rangle = [k_0, \dots, k_i, \dots, k_8]^\top, \quad (14)$$

whose members are defined as

$$|k_i\rangle = \tilde{T}^\top |f_i\rangle. \quad (15)$$

Each moment relaxes to an equilibrium state, k_i^{eq} , defined through Eq. (15) by replacing f_i with f_i^{eq} [see Eq. (5)]. The resultant expressions of the equilibrium CMs are the following:

$$\begin{aligned} k_0^{eq} &= \rho, & k_1^{eq} &= 0, \\ k_2^{eq} &= 0, & k_3^{eq} &= \rho c_s^2 \left[2 + 3(u_x^2 + u_y^2) \frac{1-\gamma}{\gamma} \right], \\ k_4^{eq} &= \rho(u_x^2 - u_y^2) \frac{1-\gamma}{\gamma}, & k_5^{eq} &= \rho u_x u_y \frac{1-\gamma}{\gamma}, \\ k_6^{eq} &= \rho u_x^2 u_y \frac{2\gamma-3}{\gamma}, & k_7^{eq} &= \rho u_x u_y^2 \frac{2\gamma-3}{\gamma}, \\ k_8^{eq} &= \rho c_s^4 \left[1 + 3(u_x^2 + u_y^2) \frac{1-\gamma}{\gamma} + 27u_x^2 u_y^2 \frac{2-\gamma}{\gamma} \right]. \end{aligned} \quad (16)$$

Similarly to the preconditioned BGK LBM [23], it can be immediately noted that these quantities reduce to the unaccelerated one if $\gamma = 1$ [37]. By relaxing the moment k_i with a frequency ω_i , the collision operator reads as follows:

$$k_i^* = k_i + \omega_i (k_i^{eq} - k_i), \quad \text{with } i = 3 \dots 8. \quad (17)$$

Only the frequencies related to k_4 and k_5 , i.e., ω_4 and ω_5 , are linked to the fluid kinematic viscosity as

$$\nu = \left(\frac{1}{\omega_{4,5}} - \frac{1}{2} \right) c_s^2 \gamma, \quad (18)$$

with $\omega_{4,5} = \omega_4 = \omega_5$. The frequency ω_3 is related to the bulk viscosity, whereas ω_6 , ω_7 , and ω_8 are associated to third- and fourth-order moments and can be set equal to 1 in order to enhance the stability of the algorithm. Notice that k_0 , k_1 , and k_2 are invariant with respect to the collision, i.e.,

$$\begin{aligned} k_0 &= k_0^{eq} = k_0^* = \rho, \\ k_1 &= k_1^{eq} = k_1^* = 0, \\ k_2 &= k_2^{eq} = k_2^* = 0. \end{aligned} \quad (19)$$

Let us collect postcollision central moments and populations as

$$|k_i^*\rangle = [\rho, 0, 0, k_3^*, \dots, k_8^*]^\top, \quad |f_i^*\rangle = [f_0^*, \dots, f_8^*]^\top, \quad (20)$$

respectively. The latter are readily available as

$$|f_i^*\rangle = (\tilde{T}^\top)^{-1} |k_i^*\rangle, \quad (21)$$

and, eventually, are streamed. In the Supplemental Material, a script [41] allows the reader to perform the symbolic manipulations to obtain all the involved quantities. Within the typical time step (from t to $t + \Delta t$), our proposed approach unravels through the following actions:

- (1) compute macroscopic variables, i.e., ρ and \mathbf{u} ;
- (2) evaluate the precollision, $|k_i\rangle$, and equilibrium, $|k_i^{eq}\rangle$, moments;
- (3) apply the collision operator to obtain $|k_i^*\rangle$;
- (4) reconstruct the postcollision population $|f_i^*\rangle$ by Eq. (21);
- (5) stream and advance in time.

A proof of consistency of our method can be shown by simple algebraic manipulations. If one poses $\omega = 1$, then the postcollision populations will match the equilibrium ones in the BGK model. A single-relaxation-time model can be derived from our proposed one by setting $\omega_i = \omega = 1$. In this case, the postcollision CMs will be equal to their equilibrium state. Now, if we reconstruct the populations, it is found that they reduce exactly to those at the equilibrium. Therefore, we have proved that the present scheme collapses perfectly into the BGK one when all the moments relax at a common rate.

1. Noncascaded approach

As mentioned in the Introduction, central moments were introduced by Geier *et al.* [27], who presented the concept of ‘‘cascaded’’ method. This name stems from the fact that the collision operator has a hierarchical structure. Conversely, our noncascaded formulation loses the orchestrated nature of the original scheme, resulting in a model possessing some very attractive features. In fact, it is very general and shows an easier-to-handle formulation, as it can be extended to any lattice velocity space. Moreover, it can be adopted to recover other different sets of equations, as shallow waters ones [42], without involving any complicated derivation. In order to exploit possible discrepancies in the results provided by the two methods, we perform a comparison in the Appendix.

The key point of our approach lies in the definition of the transformation matrix as the sum of two contributions, i.e.,

$$\tilde{T} = \mathcal{T} + \mathcal{S}. \quad (22)$$

The first term at the right hand side is computed without shifting the lattice directions by the local fluid velocity. Therefore, it represents a transformation matrix allowing us to decompose the collision operator in the space of raw moments [43]. In the D2Q9 space, the matrix \mathcal{T} reads as follows:

$$\mathcal{T} = \begin{bmatrix} 1 & 0 & 0 & 0 & 0 & 0 & 0 & 0 & 0 \\ 1 & 1 & 0 & 1 & 1 & 0 & 0 & 0 & 0 \\ 1 & 0 & 1 & 1 & -1 & 0 & 0 & 0 & 0 \\ 1 & -1 & 0 & 1 & 1 & 0 & 0 & 0 & 0 \\ 1 & 0 & -1 & 1 & -1 & 0 & 0 & 0 & 0 \\ 1 & 1 & 1 & 2 & 0 & 1 & 1 & 1 & 1 \\ 1 & -1 & 1 & 2 & 0 & -1 & 1 & -1 & 1 \\ 1 & -1 & -1 & 2 & 0 & 1 & -1 & -1 & 1 \\ 1 & 1 & -1 & 2 & 0 & -1 & -1 & 1 & 1 \end{bmatrix}.$$

Conversely, the second term accounts only for the above-mentioned shift. Clearly, one can observe that our proposed CM-based model degrades into a raw-moments-based one when $\tilde{\mathcal{T}} = \mathcal{T}$ (i.e., $\mathcal{S} = 0$). In this sense, the matrix \mathcal{S} can be interpreted as a *shift matrix*, allowing us to move from the frame at rest to the one comoving with the local fluid velocity. Notice that the matrix \mathcal{T} is related only to the desired lattice velocity space. On the other hand, the other contribution shows also a dependence on the space and time, i.e., $\mathcal{S} = \mathcal{S}(x, t)$. Aiming at developing a preconditioned scheme with raw moments, we can appreciate the versatility and generality of our scheme. In fact, the structure of the above-outlined algorithm still persists, as one needs just to replace $\tilde{\mathcal{T}}$ by \mathcal{T} . For the sake of completeness, we report in the following the equilibrium raw moments $|k_i^{eq}\rangle$:

$$\begin{aligned} k_0^{eq} &= \rho, & k_1^{eq} &= \rho u_x, \\ k_2^{eq} &= \rho u_y, & k_3^{eq} &= \rho c_s^2 [3(u_x^2 + u_y^2)\gamma^{-1} + 2], \\ k_4^{eq} &= \rho(u_x^2 - u_y^2)\gamma^{-1}, & k_5^{eq} &= \rho u_x u_y \gamma^{-1}, \\ k_6^{eq} &= \rho c_s^2 u_y, & k_7^{eq} &= \rho c_s^2 u_x, \\ k_8^{eq} &= \rho c_s^4 [3(u_x^2 + u_y^2)\gamma^{-1} + 1]. \end{aligned} \quad (23)$$

It may be immediately noted that the adoption of central moments generates the presence of third- and fourth-order velocity terms in the equilibrium terms, whereas raw ones show a dependence on the velocity up to second order.

2. Extension to the three-dimensional space

Let us demonstrate that it is possible to extend the above-outlined algorithm to the D3Q15 and D3Q27 lattice spaces, where the Eulerian basis is $\mathbf{x} = [x, y, z]$, the velocity vector is $\mathbf{u} = [u_x, u_y, u_z]$, and Eqs. (11) are completed by

$$|\bar{c}_{zi}\rangle = |c_{zi} - u_z\rangle, \quad (24)$$

$|c_{zi}\rangle$ being the components of the lattice velocities in the z direction. In the Supplemental Material, two scripts [41] allow the reader to derive the three-dimensional models. We anticipate that (similarly to the two-dimensional case) both collapse into the corresponding unaccelerated (i.e., unpreconditioned) ones if $\gamma = 1$.

First, let us focus on the D3Q15 lattice velocity space, where lattice directions are defined as

$$\begin{aligned} |c_{xi}\rangle &= [0, 1, -1, 0, 0, 0, 0, 1, -1, 1, -1, 1, -1, 1, -1]^\top, \\ |c_{yi}\rangle &= [0, 0, 0, 1, -1, 0, 0, 1, 1, -1, -1, 1, 1, -1, -1]^\top, \\ |c_{zi}\rangle &= [0, 0, 0, 0, 0, 1, -1, 1, 1, 1, 1, -1, -1, -1, -1]^\top, \end{aligned} \quad (25)$$

and the weights are $w_0 = 2/9$, $w_{1\dots 6} = 1/9$ and $w_{7\dots 14} = 1/72$. Populations and moments can be collected as

$$\begin{aligned} |f_i\rangle &= [f_0, \dots, f_i, \dots, f_l]^\top, \\ |f_i^{eq}\rangle &= [f_0^{eq}, \dots, f_i^{eq}, \dots, f_l^{eq}]^\top, \\ |f_i^*\rangle &= [f_0^*, \dots, f_i^*, \dots, f_l^*]^\top, \\ |k_i\rangle &= [\rho, 0, 0, 0, \dots, k_i, \dots, k_l]^\top, \end{aligned}$$

$$\begin{aligned} |k_i^{eq}\rangle &= [\rho, 0, 0, 0, \dots, k_i^{eq}, \dots, k_l^{eq}]^\top, \\ |k_i^*\rangle &= [\rho, 0, 0, 0, \dots, k_i^*, \dots, k_l^*]^\top, \end{aligned} \quad (26)$$

with $l = 14$. Notice that the condition

$$k_3 = k_3^{eq} = k_3^* = 0 \quad (27)$$

completes Eqs. (19). With respect to the unpreconditioned case [38], it can be noted that the algorithm implies only to change the equilibrium central moments. These quantities (in the preconditioned version) read as follows:

$$\begin{aligned} k_4^{eq} &= \rho u_x u_y \frac{1-\gamma}{\gamma}, & k_5^{eq} &= \rho u_x u_z \frac{1-\gamma}{\gamma}, \\ k_6^{eq} &= \rho u_y u_z \frac{1-\gamma}{\gamma}, & k_7^{eq} &= \rho(u_x^2 - u_y^2) \frac{1-\gamma}{\gamma}, \\ k_8^{eq} &= \rho(u_x^2 - u_z^2) \frac{1-\gamma}{\gamma}, \\ k_9^{eq} &= \rho \left[1 + (u_x^2 + u_y^2 + u_z^2) \frac{1-\gamma}{\gamma} \right], \\ k_{10}^{eq} &= \rho u_x (u_x^2 + u_y^2 + u_z^2) \frac{2\gamma-3}{\gamma}, \\ k_{11}^{eq} &= \rho u_y (u_x^2 + u_y^2 + u_z^2) \frac{2\gamma-3}{\gamma}, \\ k_{12}^{eq} &= \rho u_z (u_x^2 + u_y^2 + u_z^2) \frac{2\gamma-3}{\gamma}, \\ k_{13}^{eq} &= \rho u_x u_y u_z \frac{2\gamma-3}{\gamma}, \\ k_{14}^{eq} &= \rho c_s^2 \left[1 - (u_x^2 + u_y^2 + u_z^2) \frac{2\gamma-3}{\gamma} \right. \\ &\quad \left. + 9(u_x^2 u_y^2 + u_y^2 u_z^2 + u_x^2 u_z^2) \frac{2-\gamma}{\gamma} \right]. \end{aligned} \quad (28)$$

Now, we can derive the model for the D3Q27 space. Again, populations and CMs can be collected as in Eqs. (26) with the care of posing $l = 26$. In this case, the lattice directions are

$$\begin{aligned} |c_{xi}\rangle &= [0, 1, -1, 0, 0, 0, 0, 1, -1, 1, -1, 1, -1, 1, -1, \\ &\quad -1, 0, 0, 0, 0, 1, -1, 1, -1, 1, -1, 1, -1]^\top, \\ |c_{yi}\rangle &= [0, 0, 0, 1, -1, 0, 0, 1, 1, -1, -1, 0, 0, 0, 0, \\ &\quad 1, -1, 1, -1, 1, 1, -1, -1, 1, 1, -1, -1]^\top, \\ |c_{zi}\rangle &= [0, 0, 0, 0, 0, 1, -1, 0, 0, 0, 0, 1, 1, 1, -1, \\ &\quad 1, 1, -1, -1, 1, 1, 1, 1, -1, -1, -1, -1]^\top, \end{aligned} \quad (29)$$

with the weights set to $w_0 = 8/27$, $w_{1\dots 6} = 2/27$, $w_{7\dots 18} = 1/54$, $w_{19\dots 26} = 1/216$.

Equilibrium CMs are

$$\begin{aligned} k_4^{eq} &= \rho u_x u_y \frac{1-\gamma}{\gamma}, & k_5^{eq} &= \rho u_x u_z \frac{1-\gamma}{\gamma}, \\ k_6^{eq} &= \rho u_y u_z \frac{1-\gamma}{\gamma}, & k_7^{eq} &= \rho(u_x^2 - u_y^2) \frac{1-\gamma}{\gamma}, \\ k_8^{eq} &= \rho(u_x^2 - u_z^2) \frac{1-\gamma}{\gamma} \end{aligned}$$

$$\begin{aligned}
 k_9^{eq} &= \rho \left[1 + (u_x^2 + u_y^2 + u_z^2) \frac{1-\gamma}{\gamma} \right], \\
 k_{10}^{eq} &= \rho u_x (u_y^2 + u_z^2) \frac{2\gamma-3}{\gamma}, \\
 k_{11}^{eq} &= \rho u_y (u_x^2 + u_z^2) \frac{2\gamma-3}{\gamma}, \\
 k_{12}^{eq} &= \rho u_z (u_x^2 + u_y^2) \frac{2\gamma-3}{\gamma}, \\
 k_{13}^{eq} &= \rho u_x (u_y^2 - u_z^2) \frac{2\gamma-3}{\gamma}, \\
 k_{14}^{eq} &= \rho u_y (u_x^2 - u_z^2) \frac{2\gamma-3}{\gamma}, \\
 k_{15}^{eq} &= \rho u_z (u_x^2 - u_y^2) \frac{2\gamma-3}{\gamma}, \\
 k_{16}^{eq} &= \rho u_x u_y u_z \frac{2\gamma-3}{\gamma}, \\
 k_{17}^{eq} &= \rho c_s^2 \left[1 + 2(u_x^2 + u_y^2 + u_z^2) \frac{1-\gamma}{\gamma} \right. \\
 &\quad \left. + 9(u_x^2 u_y^2 + u_y^2 u_z^2 + u_x^2 u_z^2) \frac{2-\gamma}{\gamma} \right], \\
 k_{18}^{eq} &= \rho c_s^4 \left[1 + 6u_x^2 \frac{1-\gamma}{\gamma} + 27 \frac{2-\gamma}{\gamma} (u_x^2 u_y^2 + u_y^2 u_z^2 + u_x^2 u_z^2) \right], \\
 k_{19}^{eq} &= \rho c_s^2 (u_z^2 - u_y^2) (1 + 9u_x^2 - 18u_x^2 \gamma^{-1} - \gamma^{-1}), \\
 k_{20}^{eq} &= -\rho c_s^2 u_y u_z (1 + 9u_x^2 - 18u_x^2 \gamma^{-1} - \gamma^{-1}), \\
 k_{21}^{eq} &= -\rho c_s^2 u_x u_z (1 + 9u_y^2 - 18u_y^2 \gamma^{-1} - \gamma^{-1}), \\
 k_{22}^{eq} &= -\rho c_s^2 u_x u_y (1 + 9u_z^2 - 18u_z^2 \gamma^{-1} - \gamma^{-1}), \\
 k_{24}^{eq} &= \rho c_s^2 u_y \left[(u_x^2 + u_z^2) \frac{2\gamma-3}{\gamma} + 6u_x^2 u_z^2 \frac{2\gamma-5}{\gamma} \right], \\
 k_{25}^{eq} &= \rho c_s^2 u_z \left[(u_x^2 + u_y^2) \frac{2\gamma-3}{\gamma} + 6u_x^2 u_y^2 \frac{2\gamma-5}{\gamma} \right], \\
 k_{26}^{eq} &= \rho c_s^6 \left[1 + 3(u_x^2 + u_y^2 + u_z^2) \frac{1-\gamma}{\gamma} \right. \\
 &\quad \left. + 27(u_x^2 u_y^2 + u_y^2 u_z^2 + u_x^2 u_z^2) \frac{2-\gamma}{\gamma} + 135u_x^2 u_y^2 u_z^2 \frac{3-\gamma}{\gamma} \right],
 \end{aligned} \tag{30}$$

showing fifth- and sixth-order velocity terms. The rest of the algorithm remains totally unaltered.

III. NUMERICAL EXPERIMENTS

Here, we investigate the properties of the D2Q9 scheme outlined in Sec. II B against two well-known benchmarks, i.e., the Poiseuille flow and the lid-driven cavity. We choose these cases because they are the most popular and consolidated ones among those admitting a stationary solution. The fluid is initially at rest and the density field is initialized as $\rho(\mathbf{x}, t=0) = \rho_0$, with $\rho_0 = 1$. Moreover, velocity boundary conditions are assigned by the regularized technique [44]. We

assume that the steady state is reached when the residual error between two subsequent time steps, i.e.,

$$\epsilon(t) = \frac{\sqrt{\sum_{\mathbf{x}} [u(\mathbf{x}, t) - u(\mathbf{x}, t - \Delta t)]^2}}{\sqrt{\sum_{\mathbf{x}} u(\mathbf{x}, t)^2}} \tag{31}$$

is less than 1×10^{-12} , with $u(\mathbf{x}, t) = \sqrt{u_x(\mathbf{x}, t)^2 + u_y(\mathbf{x}, t)^2}$.

A. Poiseuille flow

A channel of length L_x and height L_y is considered. At the west and east sections, a parabolic constant horizontal rightward velocity profile is imposed in the form

$$u_x(y) = \frac{4U_0}{L_y} \left(y - \frac{y}{L_y} \right), \tag{32}$$

where $y \in [0 : L_y]$ spans the height of the channel and $U_0 = 1 \times 10^{-3}$. No-slip walls are imposed at the bottom and top sections. The Reynolds number is set to $\text{Re} = \frac{U_0 L_y}{\nu} = 100$. Let us collect the numerical solution in terms of velocity in a vertical midsection in the vector σ_{num} , whereas the vector σ_{an} stores the analytical one given by Eq. (32). Consistently, it is possible to evaluate the L_2 norm of the relative error between numerical findings and reference ones as

$$e = \frac{\|\sigma_{\text{an}} - \sigma_{\text{num}}\|}{\|\sigma_{\text{an}}\|}. \tag{33}$$

We perform a convergence analysis by varying L_y and its results are shown in Fig. 1. Different values of γ are adopted, i.e., $\gamma = 0.01, 0.05, 0.1, 0.5, \text{ and } 1$.

Except for the lowest value of the preconditioning factor, curves show an optimal convergence value of 1.98, that is fully consistent with the second-order-accurate nature of the LBM. We attribute the poor performance achieved at $\gamma = 0.01$ to the fact that the preconditioning factor should not be indefinitely reduced. In fact, the simulation becomes progressively more unstable as the effective Mach number $\text{Ma}^\dagger = U_0/c_s^\dagger$ grows [23]. Moreover, it also deprecates the accuracy of the method due to the presence of larger deleterious compressibility effects $\sim (\text{Ma}^\dagger)^2$ deviating our numerical solution from the one of the incompressible Navier-Stokes equations.

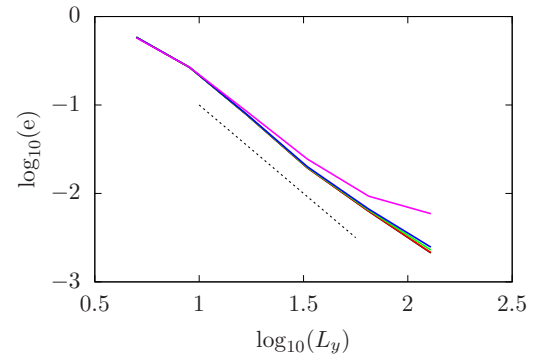


FIG. 1. Poiseuille flow: Results from a convergence analysis with $\gamma = 0.01$ (magenta), 0.05 (blue), 0.1 (green), 0.5 (red), and 1 (black). The dashed line has slope equal to -2 , corresponding to the optimal convergence rate of the LBE. To interpret the figure in a print gray-scale version, notice that the value of γ increases moving closer to the dashed line.

TABLE I. Poiseuille flow: L_2 norm of the relative error between numerical findings and analytical reference ones generated by the setups RUN1 and RUN2.

$\log_{10}(L_y)$	$\log_{10}(e)$	
	RUN1	RUN2
0.6990	-0.2338	-0.2339
0.9542	-0.5756	-0.5757
1.2304	-1.1135	-1.1136
1.5185	-1.7046	-1.7048
1.8129	-2.1878	-2.1893
2.1106	-2.6394	-2.6406
2.4099	-3.0607	-3.0611

At a first glance, the adoption of the preconditioning may lead the reader to believe that it is equivalent to run an unpreconditioned analysis at a higher value of the Mach number. However, using larger velocities can be more prone to numerical instability. On the other hand, simulations

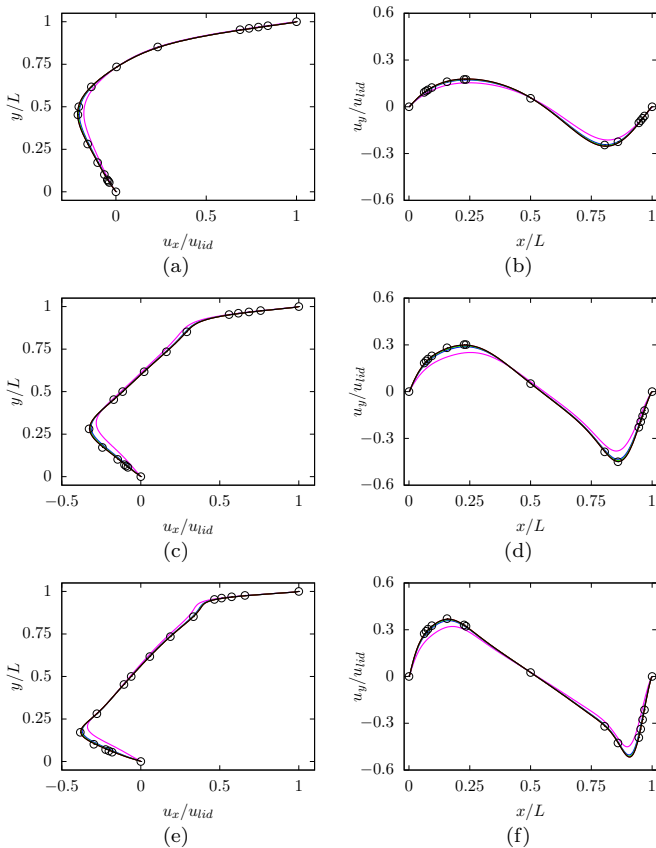


FIG. 2. Lid-driven cavity: Normalized profiles of the horizontal component of velocity in the vertical midsection (left column) and vertical component of the velocity in the horizontal midsection (right column) at $Re = 100$ (top row), 400 (central row), and 1000 (bottom row) for $\gamma = 0.01$ (magenta), 0.05 (blue), 0.1 (green), 0.5 (red), and 1 (black). Except for findings corresponding to the lowest value of the preconditioning factor, all the curves are in a very good agreement with reference benchmark values provided in [45] (circles). To interpret the figure in a print gray-scale version, notice that the value of γ increases moving closer to the circles.

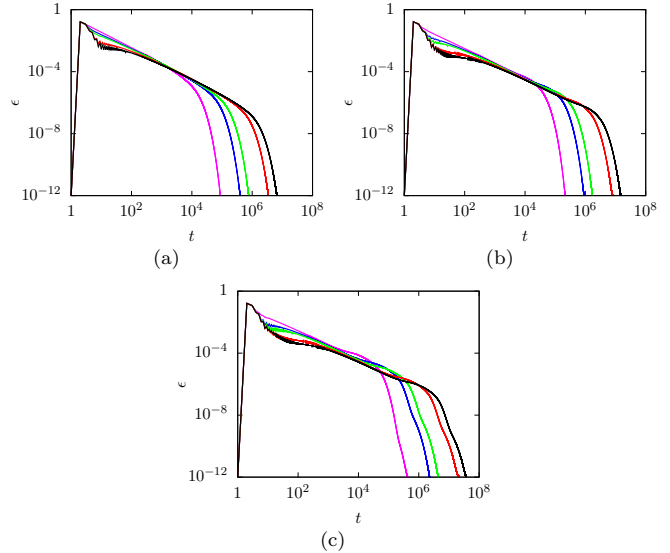


FIG. 3. Lid-driven cavity: Time evolution of the residual error ϵ for different values of γ , i.e., 0.01 (magenta), 0.05 (blue), 0.1 (green), 0.5 (red), and 1 (black), at (a) $Re = 100$, (b) $Re = 400$, and (c) $Re = 1000$. The remarkable speedup conferred by the preconditioning factor can be appreciated. To interpret the figure in a print gray-scale version, notice that the value of γ increases from left to right.

characterized by lower Mach numbers can, in particular, improve accuracy significantly by reducing compressibility errors to better represent incompressible flow. However, in such a case, the simulations can be relatively slow due to the disparities in the characteristic speeds (i.e., eigenvalue stiffness, as discussed). This can be significantly alleviated by introducing the parameter γ that leads to a tunable effective sound speed, and hence faster simulations to better represent the incompressible flow limit. To stress this point, we rerun these analyses by adopting a larger Mach number, i.e., $U_0 = 1 \times 10^{-2}$, and by setting $\gamma = 1$. In Table I, we report the values of e achieved by this setup, namely RUN1, and we compare it to the case where $U_0 = 1 \times 10^{-3}$, and $\gamma = 0.1$, namely RUN2.

In this case, the adoption of the preconditioning leads to a slight enhancement of the accuracy.

B. Lid-driven cavity

The second test involves the lid-driven cavity flow, that is known to lead to steady-state solutions if the Reynolds number

TABLE II. Lid-driven cavity: Number of time iterations t_{max} required to achieve the steady state.

γ	t_{max}		
	$Re = 100$	$Re = 400$	$Re = 1000$
0.01	88 377	214 081	429 533
0.05	399 783	900 854	2 297 688
0.1	765 730	1 725 743	4 411 387
0.5	3 461 015	8 023 043	21 407 581
1	6 605 328	14 906 996	36 943 554

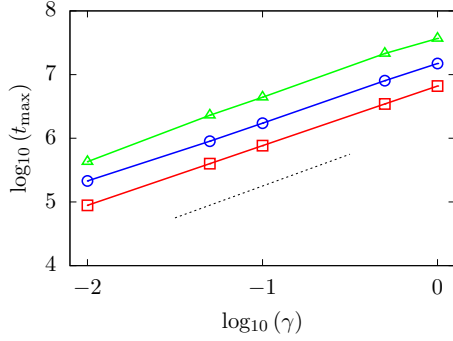


FIG. 4. Lid-driven cavity: Number of time iterations t_{\max} required to achieve the steady state at $Re = 100$ (red squares), 400 (blue circles), and 1000 (green triangles) in log-log scale. The black dashed line has slope equal to 1, highlighting that ϵ scale linearly with t_{\max} , i.e., $t_{\max} \sim \gamma$.

is lower than 7500 [45–47]. Let us consider a square domain whose sides are discretized by $L = 256$ points. A constant uniform horizontal rightward velocity $u_{lid} = 1 \times 10^{-3}$ is imposed at the top section, whereas the no-slip condition is enforced at the remaining edges. Three values of the Reynolds number, $Re = \frac{u_{lid}L}{\nu}$, are adopted, i.e., $Re = 100, 400,$ and 1000 . By varying the preconditioning factor, we depict in Fig. 2 the velocity profiles in the horizontal and vertical midsections of the cavity. In the region of the graphs with the higher curvature, findings corresponding to $\gamma = 0.01$ largely deviate from the reference values in [45]. This behavior is particularly emphasized as Re grows, due to the rise of larger velocities and velocity gradients. Conversely, the remaining curves show results that are very close to the benchmark ones in [45]. In particular, values corresponding to $\gamma = 0.5$ and 1 cannot be distinguished.

It is of interest to highlight the benefit of the preconditioning technique in terms of iterations needed to achieve the steady-state convergence. Let us plot the time history of the residual error in Fig. 3. Let us denote as t_{\max} the time instant when $\epsilon(t) < 1 \times 10^{-12}$. For the dissected range of Re and γ , this quantity is reported in Table II. It is possible to appreciate that the preconditioning technique is able to greatly reduce the number or required time iterations. The dependence of t_{\max} on γ is better highlighted in Fig. 4, where the logarithms of the two quantities are sketched. Interestingly, we find the existence of a linear dependence between the two, i.e., $t_{\max} \sim \gamma$.

This test is repeated by adopting the preconditioning BGK method devised in [23]. Let us denote as q_{BGK} and q_{CMs} the

number of iterations corresponding to a BGK run and CM-based one to reach $\epsilon < 1 \times 10^{-9}$, respectively. Consistently, we measure the (possible) speedup raised by the present method with respect to the one by Guo *et al.* [23] as

$$\delta = \frac{q_{BGK}}{q_{CMs}}. \tag{34}$$

The advantage of our model with respect to the other manifests as $\delta > 1$. The choice of a weaker threshold of the residual error is dictated by the impossibility to annihilate it much more when the BGK is adopted. In fact, this quantity tends to progressively reduce until $\epsilon \sim 10^{-9}$ and, then, it plateaus. Moreover, such a trend is particularly emphasized as $\gamma \rightarrow 1$ and Re grows. This behavior should be addressed to the presence of two concurrent causes. The former is the incidence of the round-off error, that is more prominent when Ma vanishes, as explained in [12,48]. The latter is represented by the presence of higher-order modes [49] deprecating the stability and the overall quality of the solution. While the first source of error can be alleviated by running a simulation at a higher Mach number (or better, by adopting the preconditioning as already stated), the other one requires the adoption of a more sophisticated collision operator, such as the present noncascaded central-moments-based one.

In Table III, we report the value of δ together with the number of iterations. It is observed that the difference between the two approaches is negligible at $Re = 100$. Interestingly, our proposed scheme shows faster convergence to steady state rather than the one experienced by the BGK kernel as $Re = 400$ and γ increases. Nevertheless, the real advantage of the present method arises at $Re = 1000$. Here, it reduces the number of iterations of almost one order of magnitude for the lowest value of the preconditioning factor. Moreover, the BGK operator requires more than 5×10^7 time steps to converge in the remaining case. Therefore, it is useless to adopt the BGK in these contexts, as it will involve a number of iterations considerably larger than the one required by the CM-based kernel to reach a residual error that is three orders of magnitude lower (i.e., 1×10^{-12}).

Consistently, the proposed preconditioned CM-based collision model represents an excellent candidate to perform steady-state analyses characterized by high accuracy, convergence, and stability properties.

Finally, we illustrate an example where a lid-driven cavity is considered as it possesses a nonunitary aspect ratio. Let us assume that the vertical dimension is equal to $L/2$. Moreover, the Reynolds number is set to $Re = 2000$. The contour plot of

TABLE III. Lid-driven cavity: Number of time iterations t_{\max} required to reach $\epsilon < 1 \times 10^{-9}$ by adopting the preconditioning BGK method [23] and our CM-based one. The speedup generated by the latter is denoted as δ .

γ	Re = 100			Re = 400			Re = 1000		
	CMs	BGK	δ	CMs	BGK	δ	CMs	BGK	δ
0.01	54 952	54 954	~ 1	136 896	136 915	1.0001	185 085	3 962 779	21.411
0.05	235 277	235 281	~ 1	544 753	627 374	1.1517	1 003 575	too many	
0.1	437 454	437 463	~ 1	1 007 404	1 424 871	1.4144	1 797 279	too many	
0.5	1 808 175	1 808 180	~ 1	4 190 400	6 762 098	1.6137	6 351 567	too many	
1	3 291 524	3 291 474	~ 1	7 686 059	11 753 537	1.5292	10 944 995	too many	

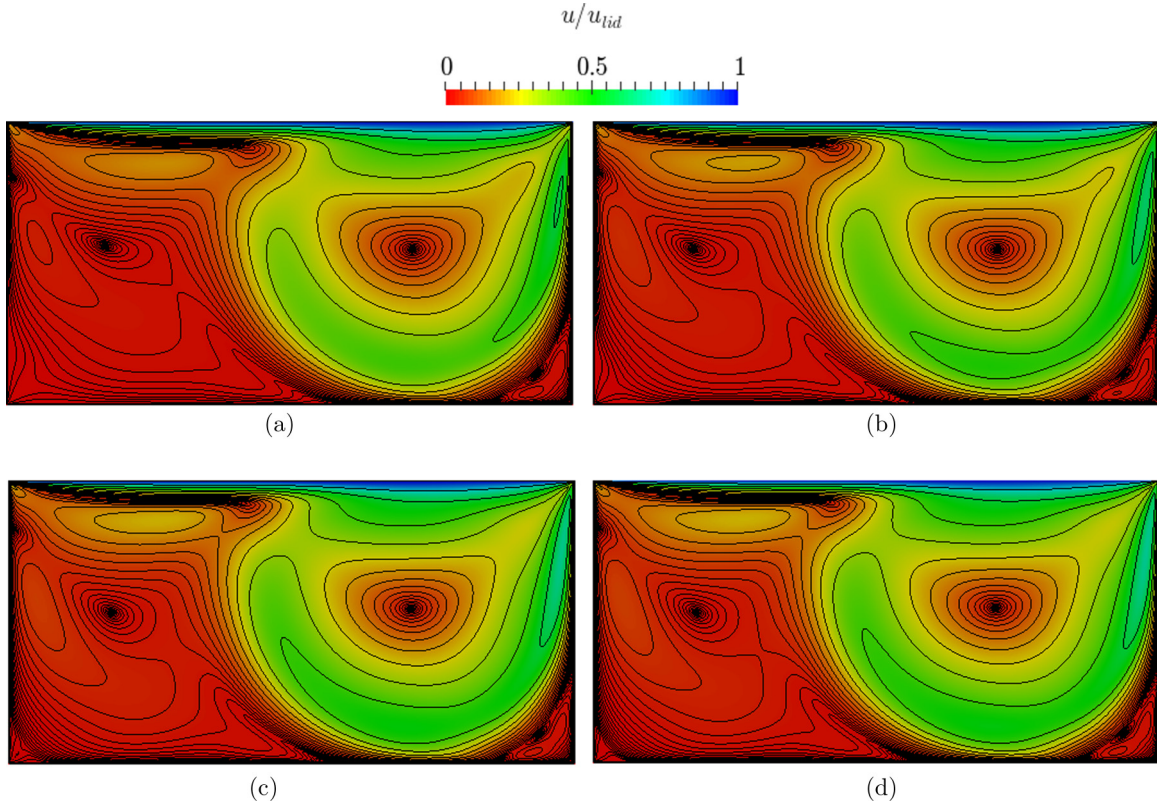


FIG. 5. Lid-driven cavity with nonunitary aspect ratio: Contour map of the magnitude of the velocity field u normalized with respect to u_{lid} at $Re = 2000$ for different values of γ , i.e., (a) 0.05, (b) 0.1, (c) 0.5, and (d) 1.

the magnitude of the velocity field is reported in Fig. 5 when the steady state is reached. Independently from the value of the preconditioning factor, our model is able to predict the existence of a main large vortex placed in the right part of the domain. More interestingly, we can capture the presence of a smaller vortical structure located in the bottom right corner of the cavity. As mentioned above, the simulation becomes more accurate as $\gamma \rightarrow 1$. Notice in fact the presence of a low-velocity region close to the rightmost section that appears progressively more prominent as γ increases.

IV. CONCLUSIONS

By adopting a nonorthogonal basis of central moments, a preconditioned central-moments-based lattice Boltzmann method has been presented. The main achievements of the present paper can be summarized as follows:

- (i) the proposed scheme is able to drastically accelerate the convergence to the steady state;
- (ii) the maximum number of iterations required to annihilate the residual error scales linearly with the preconditioning factor, i.e., $t_{max} \sim \gamma$;
- (iii) consistent with the BGK counterpart, preconditioning affects only the equilibrium state;
- (iv) the theoretical formulation is intelligible and the extension to three-dimensional lattice velocity spaces avoids any complex algebra;
- (v) all the implementations are simple.

Interestingly, our proposed methodology shows the optimal characteristics of a preconditioning technique recommended by Izquierdo and Fueyo [26].

Different from the work carried out by Hajabdollahi and Premnath [36] within the cascaded scheme, our proposed approach possesses distinct theoretical foundations. As demonstrated, the present model lies within a noncascaded framework. Our collision operator loses the pyramidal orchestrated structure characterizing the approach by Geier *et al.* [27] and two immediate consequences arise. The first is represented by a simple algorithmic procedure. The second, and more important one, is its generality as it can be developed for any lattice velocity space and can be derived for whatever BGK LBE.

ACKNOWLEDGMENTS

This article is based upon work from COST Action MP1305, supported by COST (European Cooperation in Science and Technology). The author would like to thank Prof. E. L ev eque for insightful discussions about central-moments-based schemes and Ms. F. Hajabdollahi for valuable suggestions related to preconditioning techniques. The author is also grateful to the anonymous referees, who helped to improve the quality of the manuscript with their comments.

APPENDIX: CASCADED VS NONCASCADED

Here, we present the results of a numerical test which aims at comparing the cascaded approach against the noncascaded one proposed by the author, both without preconditioning. Specifically, we elucidate their accuracy and convergence properties against the Taylor-Green vortex problem [50]. This case has been selected as it avoids the presence of velocity

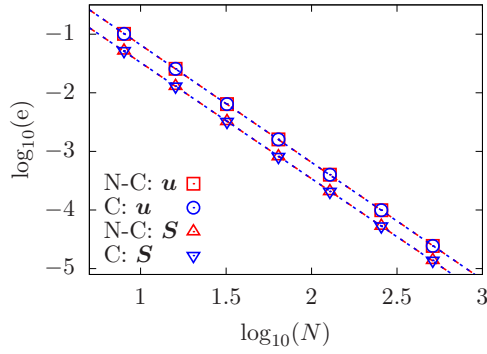


FIG. 6. Taylor-Green vortex: Results from a convergence analysis carried out by the cascaded (C) noncascaded (N-C) methods.

boundary conditions, as well as it does not involve the adoption of any forcing scheme. Consistently, it can be employed to investigate the behavior of the sole collision operators.

Let us consider a square periodic domain discretized by $N \times N$ lattice site. By imposing the following initial conditions:

$$p(\mathbf{x}, 0) = p_0 \left[1 - \frac{u_{TG}^2}{4c_s^2} [\cos(2hx) + \cos(2hy)] \right],$$

$$\mathbf{u}(\mathbf{x}, 0) = u_{TG} [\cos(hx) \sin(hy), -\sin(hx) \cos(hy)],$$

the strain rate tensor $\mathbf{S}(\mathbf{x}, t)$ and the velocity field decay with a characteristic time $T = (2h^2\nu)^{-1}$, where $u_{TG} = 0.001$, $h = 2\pi/N$, and $p_0 = \rho_0 c_s^2$. The analytical solution of the problem reads as follows:

$$\mathbf{u}(\mathbf{x}, t) = \mathbf{u}(\mathbf{x}, 0)e^{-t/T}, \tag{A1}$$

$$S_{xx}(\mathbf{x}, t) = u_{TG} h e^{-t/T} \sin(hx) \sin(hy), \tag{A2}$$

TABLE IV. Taylor-Green vortex: Logarithm of the L_2 norm of the relative error between numerical findings and analytical reference ones generated by the noncascaded method in the computation of \mathbf{u} , i.e., $e(\mathbf{u})$, and \mathbf{S} , i.e., $e(\mathbf{S})$. The convergence rate is denoted as CR and it is computed by multiplying the slope of the fitting line by -1.

$\log_{10}(N)$	$\log_{10}[e(\mathbf{u})]$	$\log_{10}[e(\mathbf{S})]$
0.9031	-0.9948	-1.2834
1.2041	-1.5919	-1.8884
1.5051	-2.1929	-2.4896
1.8062	-2.7952	-3.0888
2.1072	-3.3983	-3.6846
2.4082	-4.0027	-4.2754
2.7093	-4.6130	-4.8589
CR	2.00	1.98

$$S_{yy}(\mathbf{x}, t) = -S_{xx}(\mathbf{x}, t), \tag{A3}$$

$$S_{xy}(\mathbf{x}, t) = S_{yx}(\mathbf{x}, t) = 0. \tag{A4}$$

Let us consider a Reynolds number $Re = \frac{u_{TG} N}{\nu}$ equal to 100. We perform a convergence analysis by adopting different grid sizes, i.e., $N = [8, 16, 32, 64, 128, 256, 512]$. The L_2 norm of the relative error between numerical findings and analytical reference ones is computed by Eq. (33).

In Fig. 6, the logarithm of err is reported as a function of the logarithm of N . Both the computations of \mathbf{S} and \mathbf{u} exhibit an excellent convergence rate (see Table IV), that is fully consistent with the second-order accurate nature of the LBE. More interestingly, it must be noted that findings are overlapped, thus showing that the two share the same numerical properties.

[1] R. Benzi, S. Succi, and M. Vergassola, *Phys. Rep.* **222**, 145 (1992).
 [2] S. Succi, *Europhys. Lett.* **109**, 50001 (2015).
 [3] S. Succi, *Philos. Trans. R. Soc. A* **374**, 20160151 (2016).
 [4] S. Ubertini, P. Asinari, and S. Succi, *Phys. Rev. E* **81**, 016311 (2010).
 [5] P. Bhatnagar, E. Gross, and M. Krook, *Phys. Rev.* **94**, 511 (1954).
 [6] A. J. Ladd, *J. Fluid Mech.* **271**, 285 (1994).
 [7] H. Chen, S. Kandasamy, S. Orszag, R. Shock, S. Succi, and V. Yakhot, *Science* **301**, 633 (2003).
 [8] H. Yu, S. S. Girimaji, and L.-S. Luo, *Phys. Rev. E* **71**, 016708 (2005).
 [9] M. Krafczyk, J. Tölke, E. Rank, and M. Schulz, *Comput. Struct.* **79**, 2031 (2001).
 [10] Z.-G. Feng and E. Michaelides, *Comput. Fluids* **38**, 370 (2009).
 [11] A. De Rosi, *Comput. Struct.* **153**, 230 (2015).
 [12] T. Krüger, H. Kusumaatmaja, A. Kuzmin, O. Shardt, G. Silva, and E. M. Viggien, *The Lattice Boltzmann Method: Principles and Practice* (Springer, New York, 2016).
 [13] S. Succi, *The Lattice Boltzmann Equation for Fluid Dynamics and Beyond* (Clarendon, Oxford, 2001).
 [14] R. Verberg and A. J. C. Ladd, *Phys. Rev. E* **60**, 3366 (1999).
 [15] M. Bernaschi, S. Succi, and H. Chen, *J. Sci. Comput.* **16**, 135 (2001).
 [16] J. Tölke, M. Krafczyk, and E. Rank, *J. Stat. Phys.* **107**, 573 (2002).
 [17] D. Kandhai, A. Koponen, A. Hoekstra, and P. M. Sloot, *Future Gen. Comput. Syst.* **18**, 89 (2001).
 [18] T. Lee and C.-L. Lin, *J. Comput. Phys.* **185**, 445 (2003).
 [19] T. Seta and R. Takahashi, *J. Stat. Phys.* **107**, 557 (2002).
 [20] J. Tölke, M. Krafczyk, M. Schulz, E. Rank, and R. Berrios, *Int. J. Mod. Phys. C* **9**, 1143 (1998).
 [21] D. J. Mavriplis, *Comput. Fluids* **35**, 793 (2006).
 [22] E. Turkel, *Annu. Rev. Fluid Mech.* **31**, 385 (1999).
 [23] Z. Guo, T. S. Zhao, and Y. Shi, *Phys. Rev. E* **70**, 066706 (2004).
 [24] K. N. Premnath, M. J. Pattison, and S. Banerjee, *J. Comput. Phys.* **228**, 746 (2009).
 [25] S. Izquierdo and N. Fueyo, *Prog. Comput. Fluid Dyn.* **8**, 189 (2008).
 [26] S. Izquierdo and N. Fueyo, *J. Comput. Phys.* **228**, 6479 (2009).
 [27] M. Geier, A. Greiner, and J. G. Korvink, *Phys. Rev. E* **73**, 066705 (2006).
 [28] M. Geier, A. Greiner, and J. Korvink, *Int. J. Mod. Phys. C* **18**, 455 (2007).

- [29] M. Geier, *Int. J. Numer. Methods Fluids* **56**, 1249 (2008).
- [30] P. Asinari, *Phys. Rev. E* **78**, 016701 (2008).
- [31] M. Geier, A. Greiner, and J. Korvink, *Eur. Phys. J.: Spec. Top.* **171**, 55 (2009).
- [32] K. N. Premnath and S. Banerjee, *Phys. Rev. E* **80**, 036702 (2009).
- [33] K. Premnath and S. Banerjee, *J. Stat. Phys.* **143**, 747 (2011).
- [34] Y. Ning, K. N. Premnath, and D. V. Patil, *Int. J. Numer. Methods Fluids* **82**, 59 (2016).
- [35] M. Geier, M. Schönherr, A. Pasquali, and M. Krafczyk, *Comput. Math. Appl.* **70**, 507 (2015).
- [36] F. Hajabdollahi and K. N. Premnath, *Comput. Math. Appl.* (2017).
- [37] A. De Rosis, *Europhys. Lett.* **116**, 44003 (2016).
- [38] A. De Rosis, *Phys. Rev. E* **95**, 013310 (2017).
- [39] A. De Rosis, *Phys. Rev. E* **95**, 023311 (2017).
- [40] A. De Rosis, *Europhys Lett.* **117**, 34003 (2017).
- [41] See Supplemental Material at <http://link.aps.org/supplemental/10.1103/PhysRevE.96.063308> for performing all the computations to obtain k_i , k_i^{eq} , and f_i^* , as well as for performing all the computations to derive the three-dimensional models
- [42] A. De Rosis, *Comput. Method. Appl. M.* **319**, 379 (2017).
- [43] D. d’Humières, *Philos. Trans. R. Soc., A* **360**, 437 (2002).
- [44] J. Latt, B. Chopard, O. Malaspinas, M. Deville, and A. Michler, *Phys. Rev. E* **77**, 056703 (2008).
- [45] U. Ghia, K. N. Ghia, and C. Shin, *J. Comput. Phys.* **48**, 387 (1982).
- [46] O. Botella and R. Peyret, *Comput. Fluids* **27**, 421 (1998).
- [47] C.-H. Bruneau and M. Saad, *Comput. Fluids* **35**, 326 (2006).
- [48] P. A. Skordos, *Phys. Rev. E* **48**, 4823 (1993).
- [49] J. Latt and B. Chopard, *Math. Comput. Simul.* **72**, 165 (2006).
- [50] G. Taylor and A. Green, *Proc. R. Soc. London, Ser. A* **158**, 499 (1937).